

# Chemical Bonding in Metallic Glasses from Machine Learning and Crystal Orbital Hamilton Population

Ary R. Ferreira\*

Department of Physics, Universidade Federal de São Carlos (UFSCar), 13565-905, São Carlos, SP, Brazil

(Dated: September 12, 2022)

The chemistry (composition and bonding information) of metallic glasses (MGs) is at least as important as structural topology for understanding their properties and production/processing peculiarities. This article reports a machine learning (ML)-based approach that brings an unprecedented “big picture” view of chemical bond strengths in MGs of a prototypical alloy system. The connection between electronic structure and chemical bonding is given by crystal orbital Hamilton population (COHP) analysis within the framework of density functional theory (DFT). The stated comprehensive overview is made possible through a combination of efficient quantitative estimate of bond strengths supplied by COHP analysis, representative statistics regarding structure in terms of atomic configurations achieved with classical molecular dynamics simulations, and the smooth overlap of atomic positions (SOAP) descriptor. The study is supplemented by an application of that ML model under the scope of mechanical loading, in which predicted bond strengths enabled atom categorization based on a descriptor of the short-range order possessing a superior chemical sense; a key component to uncover structural/chemical heterogeneity and its influence on mechanical relaxation processes and atomic scale flow mechanisms in MGs.

## I. INTRODUCTION

Since early reports of glassy alloys, over almost 60 years ago [1], their importance within the broad scope of technological developments of metallic materials has grown noticeably, although such pertinence has apparently reached a threshold in last decade [2]. Metallic glasses (MGs) are amorphous alloys that exhibit a glass transition and are notorious for their extreme hardness and strength; thus they became obvious candidates for structural applications, while other relevant usage proposals have already been put forward like in biomedicine, nanotechnology, energy, and microelectromechanical systems [3, 4]. Yet, at the present time, research and development (R&D) activities related to this class of advanced materials are still facing challenging issues such as critical casting thickness or brittleness of some nominal compositions found to be good glass formers. Nevertheless, recent advances in basic and applied research have provided innovative strategies for designing new MGs, with the focus on enhanced mechanical, chemical, and magnetic properties. For example, 3D printing (or additive manufacturing) is emerging as a promising alternative for the fabrication of Fe-based MGs parts to be employed as magnetic shielding or transformer (electrical device) core laminations [5, 6]. Another prospect, relevant for energy applications, is the synthesis of MGs with large specific surface areas, which were found to be efficient for ultra-fast hydrogen uptake [4].

Technological developments in characterization techniques were crucial to promote insights into the structure of multicomponent MGs at the atomic, microscopic, and nanoscopic scales. Down to the atomistic scale, the

lack of long-range crystalline order – perchance associated with nontrivial chemistry – makes it a hard task to uncover mechanisms underlying transformations that occur in two essential contexts: (i) the former is the production process of MGs, what requires mastery of key formation mechanisms that determine glass-forming ability (GFA); (ii) the other scenario is application and, concerning their most prominent usability as structural materials [7], recent efforts have been focused on unveiling defects likely to determine mechanical behavior, in close analogy to well-known plastic flow mechanisms existing in crystalline systems. Particularly in this latter context, recent basic research has been conducted into atomic-scale characterization of structural heterogeneity [8] and dynamic ‘defects’ from the perspective of *flow units* [9]. This is an aspect of MGs that reflects their space-time heterogeneity and a technique that has been increasingly used to study the associated relaxation dynamics is dynamical mechanical analysis (DMA, aka dynamical mechanical spectroscopy), due to its high sensitivity in detecting atomic rearrangements [10–14].

Still regarding structural characterization, large-scale molecular dynamics (MD) simulations have proven effective in providing trustworthy structural models able to reproduce properties of MGs like density, glass transition temperature, and representative statistics regarding atomic configurations [15]. Even so, the problematic issue of using MD simulations within that scope is that structural models containing at least some thousands of atoms are required for most MGs; even for the prediction of “static” features like short- and medium-range orders (SRO and MRO). This is a constraint that imposes a critical limitation on the use of *ab initio* quantum mechanical MD simulations for that end and the solution is also not new. It consists of a multiscale approach, in which the role of electrons on interatomic interactions is abstracted and described in terms of the so-called in-

\* ary.ferreira@df.ufscar.br

teratomic potentials employed in classical MD (CMD) simulations. However, a manifest disadvantage in this approach is that so many additional properties originating from electronic structure – other than interatomic interactions – become simply not accessible in large-scale CMD simulations.

This article reports an unprecedented “big picture” view of chemical bond strengths in MGs of the Zr–Cu–Al (ZCA) alloy system. The link between electronic structure and first-principles chemical bonding information is given by density functional theory (DFT) [16, 17] and crystal orbital Hamilton population (COHP) analysis [18], whereas representative statistics is attained by applying a machine learning (ML) approach to structural models generated by CMD simulations. The resulting overview of chemical interactions allowed qualitative and quantitative analysis of deformation behavior from the perspective of concepts currently used to describe structural heterogeneity and atomic-scale flow mechanisms in these MGs. Among which stand out: the so-termed *weakest configurations* [19], conceived as well-defined less stiff regions supposed to exist in the solid bulk; *bond exchange* [20] processes to which weakly bonded atoms within these regions would be more susceptible as marked rearrangements; and the current broader notion of *flow units* [9], which are defined as regions that mainly contribute to the viscoelastic features of MGs.

## II. THEORY AND COMPUTATIONAL DETAILS

### A. The Machine Learning-Based Approach

The ZCA alloy was selected as a model alloy for the proposed ML-based approach because of its practicality. First of all, its MGs are conventional prototypical systems extensively studied due to their high GFA [21]; and there are plenty of experimental and theoretical works available in the literature covering different topics on them. Moreover, the computational modeling process is made easy for this alloy given the availability of an interatomic potential [15] which has been widely tested for years, yielding fair agreement with ordinary experimental properties [22]. Additionally, it provides plausible description of “static” bulk SRO and MRO in these MGs with affordable 10000-atoms cells [15] – assuming, naturally, a homogeneous distribution of constituent atoms, i.e., a microstructure free of nanocrystals [4, 23]. In order to draw a parallel between theoretical findings from the present work and experiments reported in the literature, the same set of four nominal compositions (NCs)  $(\text{Zr}_{0.5}\text{Cu}_{0.5})_{100-x}\text{Al}_x$  (with  $x = 2, 6, 8$ , and 10) studied in Ref. 23 was taken as a primary model alloy.

The precise motivation for a ML-based approach here is to enable the prediction of bond strengths between atom pairs with the DFT accuracy, but in 10000-atoms cells of the ZCA MGs derived from CMD simulations. Such cells are expected to supply representative statis-

TABLE I. Overview in numbers of the per-type DBIs created for the MGs using the 100-atoms cells generated following the quenching protocol described in the text and whose amounts are indicated in the last row. All cells are available in the Supporting Information as *extended XYZ* files.

	Zr <sub>49</sub> Cu <sub>49</sub> Al <sub>2</sub>	Zr <sub>47</sub> Cu <sub>47</sub> Al <sub>6</sub>	Zr <sub>45</sub> Cu <sub>45</sub> Al <sub>10</sub>
Al–Al	27	64	552
Cu–Al	5080	1775	17073
Cu–Cu	57230	6311	32859
Zr–Al	7011	2497	22938
Zr–Cu	169487	19153	99015
Zr–Zr	76919	8558	43547
100-atoms cells	488	58	326

tics regarding SRO (chemical environments) in these systems however, it is manifest that the corresponding electronic structure quantum mechanical simulations is something unfeasible and unnecessary. This is where the proposed ML model comes onto the scene, by learning bond strengths from a database of interactions (DBIs). The strategy for the generation of the required number of structures to train the ML model was grounded on the assumption that the referred statistical representativeness existing in a 10000-atoms cell of a given NC, can be attained with an ensemble of smaller 100-atoms cells of the same NC. As described in details in Section II B, all these cells were obtained by CMD simulated cooling from the melt and the referred statistical equivalence was indeed achieved (see Supporting Information).

Hence, in order to train the proposed ML model, a set of per-type DBIs has been created for all possible interaction types (ITs): Al–Al, Cu–Al, Cu–Cu, Zr–Al, Zr–Cu, and Zr–Zr. Table I brings out an overview in numbers of these databases and details on their creation are provided in Section II B; including strategies for diversifying the collection of chemical environments and to ensure transferability among different NCs. Here, it has to be pointed that the small number of Al–Al interactions shown in Table I is intrinsic to the material. It follows upon microalloying of Al and it has already been described in the literature as a *solute–solute avoidance* effect [24, 25]. As discussed in the Supporting Information, concerning the abovementioned transferability, it was not a complicating factor when further applying the ML model, and a single Al–Al DBI was set up by merging the three related DBIs listed in Table I.

Each individual interaction in the set of DBIs must have an associated bond strength value and, as already introduced, chemical bonding information from first-principles can be attained from COHP analysis. In short, a COHP curve is calculated for a given pair-wise interaction and its integral up to the Fermi level (ICOHP) can be taken as a quantitative measure of bond strength. More details regarding the use of this method are outlined in Section II B and the projected COHP (pCOHP) approach [26, 27] was adopted as implemented in the LOBSTER code [28, 29].

At this point, it is appropriate to introduce a key “ingredient” of the proposed ML model, whose versatility also allowed the assessment of the convergence of SRO statistics in the 100-atoms cells in advance. It refers to the mathematical descriptor of each chemical environment around an individual atom, necessary to measure the “distance” (or dissimilarity) between atomic environments. The descriptor adopted in the present work is the smooth overlap of atomic positions (SOAP) [30] and the corresponding vectors were generated using the QUIP package [31]. In practice, the normalized similarity between such SOAP vectors computed for two atoms,  $i$  and  $j$ , is given by their dot product,  $\mathbf{q}_i \cdot \mathbf{q}_j$ .

$$k(B_m, B_n) = \exp \left( -\frac{(d_{ij}^m - d_{ij}^n)^2}{2\theta^2} \right) \left( \frac{(\mathbf{q}_i^m \cdot \mathbf{q}_i^n + \mathbf{q}_j^m \cdot \mathbf{q}_j^n + \mathbf{q}_i^m \cdot \mathbf{q}_j^n + \mathbf{q}_j^m \cdot \mathbf{q}_i^n)}{4} \right). \quad (1)$$

With  $d_{ij}^m$  the distance between atoms  $i$  and  $j$  in the chemical bond  $B_m$ , and  $\mathbf{q}_i^m$  and  $\mathbf{q}_j^m$  their corresponding SOAP vectors. The adjustable scaling parameter  $\theta$  defines the ML model’s behavior and sets the characteristic length-scale of the GPR.

Finally, by using the *kernel* function in equation 1, the ML model is then able to predict the ICOHP value associated to an arbitrary bond  $B$  by following

$$ICOHP^{ML}(B) = \sum_{m=1}^N \alpha_m k(B, B_m)^\zeta. \quad (2)$$

With the hyperparameter  $\zeta = 1$  establishing a linear *kernel*, and  $N$  the size of the training DBI at issue containing the set of reference chemical bonds  $\{B_m\}_{m=1}^N$  (or training set) with their corresponding *ab initio* ICOHP values. By inverting the  $N \times N$  *kernel* matrix  $\mathbf{K}$ , whose elements  $K_{mn} = k(B_m, B_n)$  are defined with the training set, the per-interaction weights  $\alpha_m$  in equation 2 are computed according to

$$\alpha_m = \sum_{n=1}^N \{\mathbf{K}^\zeta + [(\sigma^2 \gamma) \mathbf{1}]\}_{mn}^{-1} ICOHP^{DFT}(B_n). \quad (3)$$

With  $\sigma^2$  the standard deviation of the ICOHP values in the training set  $\{B_n\}_{n=1}^N$ ,  $\gamma$  a regularization adjustable parameter,  $\mathbf{1}$  the  $N \times N$  unit matrix, and  $ICOHP^{DFT}(B_n)$  the ICOHP value of the reference chemical bond  $B_n$  computed from first-principles.

## B. Computational Details

All the CMD simulations were carried out using the velocity-Verlet integrator as implemented in the LAMMPS package [32] (release 16Feb2016). The embedded atom model (EAM) interatomic potential developed and extensively tested by Cheng *et al.* [15, 33] was

Turning to the specification of the ML model, it is important to remark that its implementation is not intended to predict atomic (or per-atom) scalar quantities. The ICOHP is a scalar property that is associated to atom pairs and, since the proposed ML model is founded upon a Gaussian process regression (GPR) framework, the function that measures the similarity between two chemical bonds (the *kernel* function  $k(B_m, B_n)$ ) has to take into account two basic features: bond distances and the individual SOAP vectors of the atoms involved. Thus, the covariance (or *kernel*) function was defined as a squared exponential weighted by the normalized similarities given by the referred SOAP vectors, as following

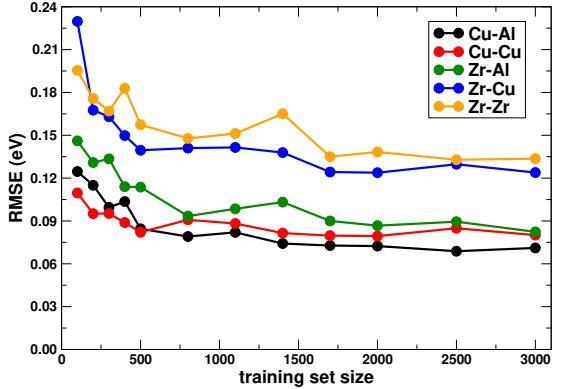


FIG. 1. Root-mean-square errors (RMSE) calculated from different Gaussian process regressions made for each interaction type in the nominal composition  $Zr_{45}Cu_{45}Al_{10}$  assuming distinct training set sizes. The ML model parameters were set as  $\zeta = 1$ ,  $\theta = 0.5$ , and  $\gamma = 0.010$ , and a fixed testing set size of 1000 interactions was taken.

used with a cutoff radius of 6.5 Å to describe the interatomic forces in all MGs. A common quenching protocol was used for the generation of all 10000-atoms and 100-atoms cells introduced in Section II A. Firstly, an initial configuration was set by randomly positioning the atoms in a cubic supercell, whose initial volume was estimated for each NC by initially assuming a dense sphere packing weighted with the Zr, Cu, and Al atomic radii, with a length in excess of 10% added to each cell vector. In order to avoid superposition of atoms, a conjugate gradient minimization on the random initial structure was executed with a stop criterion defined by a force threshold of  $10^{-8}$  eV/Å. Next, the system was thermalized at 2000 K in the isothermal-isobaric (*NPT*) ensemble for 2 ns, in the time evolution of the CMD simulation ( $\Delta t$ ). With a time step of 2 fs, adopted in all runs, the Nosé-

Hoover thermostat was used with a dump coefficient of 0.2 ps, whereas the barostat was set to zero pressure with a dump coefficient of 2 ps. Subsequently, the system was cooled to 300 K with a minimal and feasible rate of  $8.5 \times 10^9$  K/s. And finally, the glassy structure was allowed to relax at 300 K for  $\Delta t = 2$  ns.

As pointed out in Section II A, some of the 100-atoms cells listed in Table I were submitted to DFT first-principles calculations for setting up the DBIs for the ML model – they were carried out on demand. For the purpose of diversifying the collection of chemical environments, each one of those selected cubic supercells derived from CMD simulations was submitted to 3D geometrical transformations that generated 14 new structures, namely: shearing along the x, y, and z axes (6 new structures); compression and tension along the x, y, and z axes (6 new structures); isotropic compression and tension (2 new structures).

All the referred DFT electronic structure simulations were performed using the QUANTUM ESPRESSO [34, 35] (QE) open-source software suite version 6.2.0, with plane-wave (PW) basis sets and projector augmented waves (PAW) [36] datasets from the PSLibrary project version 1.0.0 [37]. The Perdew-Burke-Ernzerhof (PBE) [38] generalized gradient approximation was used to describe the exchange-correlation functional in all computations. Remarking that the abovementioned EAM interatomic potential [15, 33] used in the CMD simulations was also parametrized from results of DFT-PBE calculations. For all 100-atoms cells, the PW basis set was truncated with a kinetic energy cutoff of 70 Ry and the Monkhorst-Pack procedure [39] was used to determine the k-points disposition in the first Brillouin zone from a  $2 \times 2 \times 2$  sampling. A Fermi-Dirac probability distribution was used as a smearing function to set the occupations of energy levels, with a common broadening parameter  $k_b T = 8$  mRy.

The ICOHP values for the interactions listed in Table I and selected to compose the DBIs, were computed within the pCOHP approach [26, 27] as implemented in the LOBSTER code [28, 29] version 3.0.0. This method allows the transfer of chemical bonding related quantum mechanical information from reciprocal space, to a pairwise local orbitals interaction language. This is nothing but an alternative way to apply a “filter” to a density of states (DOS) curve, in order to obtain a spatial and/or atomic orbital-resolved view of it. A pCOHP curve tells whether atomic orbitals centered at neighboring sites are bonding, non-bonding or antibonding in the same energy range of a projected DOS counterpart. Its energy-integration up to the Fermi level (the ICOHP value) yields a measure of chemical bonding strength and a detailed description of the general approach to apply this method within the PAW framework is available in Ref. 27. The default local basis set provided by Bunge *et al.* [40] were used for projections, with the following set of local orbitals for each atomic specie: Al ( $3s\ 3p_x\ 3p_y\ 3p_z$ ); Cu ( $3s\ 4s\ 3p_x\ 3p_y\ 3p_z\ 3d_{xy}\ 3d_{yz}\ 3d_{zx}\ 3d_{xz}\ 3d_{x^2-y^2}$ ); and

Zr ( $4s\ 5s\ 4p_x\ 4p_y\ 4p_z\ 4d_{xy}\ 4d_{yz}\ 4d_{zx}\ 4d_{xz}\ 4d_{x^2-y^2}$ ).

The SOAP descriptors were generated using the QUIP package [31], with a cutoff of 3.75 Å for the definition of the range of each chemical environment around atoms, including all elements in its composition. This cutoff value was based on partial pair distribution functions that are well-known for the MGs of the ZCA alloy [15]. The spherical harmonics basis band limit and the number of radial basis functions were set to 6 and 8, respectively. All the remaining parameters were set with their default values.

### III. RESULTS AND DISCUSSION

#### A. Predictive Power of the ML Model

The predictive power of the ML model given by equation 2 was evaluated individually for each interaction type (IT) by studying its convergence with respect to the training set size, for a fixed testing set size. Due to its completeness (see Table I), the set of DBIs created for the NC Zr<sub>45</sub>Cu<sub>45</sub>Al<sub>10</sub> was selected for initial tests, whose results are presented in Fig. 1 and for which the ML model parameters were arbitrarily set as  $\zeta = 1$ ,  $\theta = 0.5$ , and  $\gamma = 0.010$  (see also equations 1 and 3). It can be seen in Fig. 1 that the corresponding root-mean-square errors (RMSE) are dependent on the IT but, in general, they are fairly converged with small training set sizes (from about 500 interactions). Furthermore, given the range of -ICOHP values computed for the MGs under study (see Table S1), the individual RMSE values calculated for each IT show that the ML model produces small prediction errors. Remarking that each point in the plots of Fig. 1 corresponds to a GPR in which the training and testing sets were randomly created from the DBIs listed in Table I. Moreover, it has to be informed that the conventional additive inverse of ICOHP (-ICOHP) to indicate bond strengths was adopted, so that positive and negative values of the corresponding COHP functions define bonding and antibonding contributions, respectively [26].

Table S1 provides further statistics from a set of GPRs equivalent to those shown in Fig. 1, however adopting rather large training and testing sets. As already mentioned, the lack of Al-Al interactions is intrinsic to the ZCA alloy and made it impossible to carry out the same thorough tests for that specific IT. Nevertheless, it can be checked in Table S1 that the corresponding RMSE values also point to small prediction errors. Regarding the other two NCs Zr<sub>47</sub>Cu<sub>47</sub>Al<sub>6</sub> and Zr<sub>49</sub>Cu<sub>49</sub>Al<sub>2</sub>, it can be verified in Tables S2 and S3 that similar RMSE values were found for their correlated DBIs. Hence, since RMSE values are scale-dependent, the overall predictive power of the proposed ML model can be said satisfactory within the context of this study. The scatter plots of some particular ITs listed in Table S1 are shown in Fig. 2 and the complete list is available in the Supporting Information (Figs. S13 to S30).

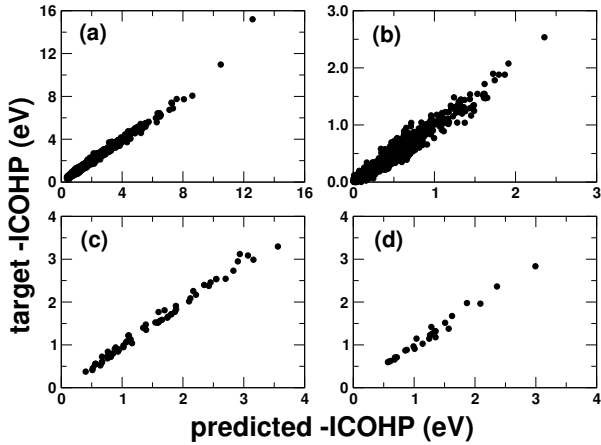


FIG. 2. Scatter plots of results from some of the Gaussian process regressions listed in Table S1: (a) Zr–Zr in  $Zr_{45}Cu_{45}Al_{10}$ ; (b) Cu–Cu in  $Zr_{45}Cu_{45}Al_{10}$ ; (c) Al–Al in  $Zr_{47}Cu_{47}Al_6$ ; and (d) Al–Al in  $Zr_{49}Cu_{49}Al_2$ .

### B. Application of the ML Model

Once the validation is complete, the ML-based approach was used to predict bond strengths between atom pairs in the four 10000-atoms cells created for each NC of the ZCA alloy. Based on the convergence tests and transferability of individual DBIs explained in the Supporting Information, it was defined a minimal and feasible training set  $(\{B_n\}_{n=1}^N)$  with 600 interactions for each IT, by merging equally the corresponding DBIs of the three NCs listed in Table I. These 10000-atoms cells are able to provide the required statistical representativeness regarding chemical environments in these MGs and were generated with CMD simulations following the protocol described in Section II B.

*Weakest configurations* [19], *bond exchange* [20] processes, and *flow units* [9] were introduced as current conceptions that treat MGs's atomic structure from a point of view in which weakly bonded (WB) atoms play a key role. Substantially, they bring the picture of an alloy composed by atomic motifs formed by strongly bonded (SB) atoms – also already described in the literature as an *elastic-like* matrix – in which *liquid-like* portions of the solid made up of WB atoms [9] are immersed. Such perspective naturally suggests a heterogeneous spatial distribution of chemical bond strengths and meets the goal in the present work. However, instead of going straight to the issue of how -ICOHP values are distributed within the 10000-atoms cells, it is worth looking first at simpler per-IT statistics, as depicted in Fig. 3.

Above all, it should be emphasized that the set of results in Fig. 3 represents an unprecedented “big picture” view of bond strengths between atoms in these MGs derived from quantum mechanics. With respect to chemical bonding information, that comprehensive overview is arguably more complete and revealing than previous reports with similar aims, including quantum chemistry

TABLE II. Groupings of atoms in the 10000-atoms cells of the ZCA alloy based on  $\langle -ICOHP \rangle_{ref} = 1.00$  eV (see text).

	$Zr_{49}Cu_{49}Al_2$	$Zr_{47}Cu_{47}Al_6$	$Zr_{46}Cu_{46}Al_8$	$Zr_{45}Cu_{45}Al_{10}$
$Cu_{WB}$	4895	4687	4590	4487
$Cu_{SB}$	5	13	10	13
$Zr_{WB}$	1729	1694	1713	1685
$Zr_{SB}$	3171	3006	2887	2815
$Al_{WB}$	0	0	0	0
$Al_{SB}$	200	600	800	1000

calculations with localized basis sets for rather small isolated atomic clusters [41, 42], or even DFT-MD simulations carried out with periodic boundary conditions, but for cells containing a few hundred interatomic interactions [15]. In fact, the profiles of the distributions in Fig. 3 do not exhibit significant changes upon microalloying of Al and, as expected, only their correlated fractions vary distinctively in each IT (indicated as percentages). Nevertheless, they suggest that atoms can be grouped according to their chemical bonding situations, enabling a segregation between WB and SB atoms based on a given reference -ICOHP value. This is reasonable indeed, and one can see that Cu–Cu interactions show up as the weakest ones, together with a non-negligible fraction of Zr–Cu and Zr–Zr bonds, all having -ICOHP values below around 0.8 eV. Conversely, a substantial number of relatively strong Zr–Cu and Zr–Zr bonds is predicted by the ML model. Moreover, one further remark concerning the effect of microalloying of Al is that, although the negligible amount of Al–Al bonds, due to the already introduced *solute–solute avoidance* effect [24, 25], a fair number of strong Zr–Al and Cu–Al interactions (with  $-ICOHP \gtrsim 1.0$  eV) rise.

Since the matter at issue involves atoms in different chemical bonding situations, the ML-predicted per-bond -ICOHP values were used to compute a set of per-atom average  $\langle -ICOHP \rangle$  values for each NC – the arithmetic mean taken over the strengths of the bonds between a central atom and its first-neighbors. Next, based on tests well described and discussed in the Supporting Information, atoms were grouped according to their bonding situations (WB and SB atoms) for each specie (Zr, Cu, and Al), based on an optimal  $\langle -ICOHP \rangle$  reference value  $\langle -ICOHP \rangle_{ref} = 1.0$  eV, as listed in Table II. Table S4 shows for the NC  $Zr_{45}Cu_{45}Al_{10}$  that, by assuming different  $\langle -ICOHP \rangle_{ref}$  values, it is possible to split atoms into two individual groups for each specie: WB, with those for which  $\langle -ICOHP \rangle \leq \langle -ICOHP \rangle_{ref}$ ; and SB, containing the remainder.

So, the next target is a first evidence that the groups of atoms listed in Table II indeed represent a rational partition of the MG's bulk structure into *weakest configurations* (or WB atoms) and remaining SB atoms. Fig. 4 shows the distribution of atoms in different bonding situations lying within two arbitrary and representative 2.5 Å slabs, which were taken from the 10000-atoms cells of the NCs  $Zr_{49}Cu_{49}Al_2$  and  $Zr_{45}Cu_{45}Al_{10}$  (see Fig. S37 in

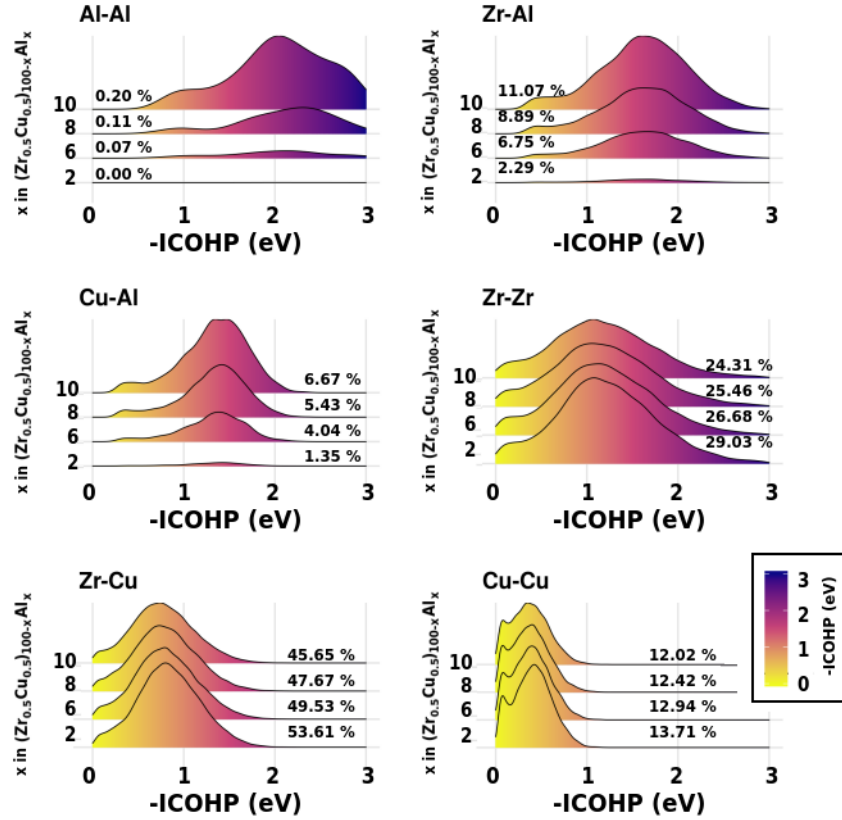


FIG. 3. Distributions of -ICOHP values predicted by the ML model for all interatomic interactions existing in 10000-atoms cells of the series of nominal compositions (NC)  $(\text{Zr}_{0.5}\text{Cu}_{0.5})_{100-x}\text{Al}_x$  (with  $x = 2, 6, 8$ , and  $10$ ). The fractions of each interaction type (IT) in each NC are indicated as percentages.

the Supporting Information about the referred representativeness). In fact, the distribution of WB atoms in the structure of the MG  $\text{Zr}_{49}\text{Cu}_{49}\text{Al}_2$ , as shown in Fig. 4(b), resembles a matrix of *weakest configurations* involving the so-called *string-like* configurations composed by SB atoms presented in Fig. 4(c). Whereas, the opposite picture is normally suggested in the literature, i.e., *liquid-like* cores surrounded by an elastic matrix [8]. However, it is important to stress that the used partition criterion  $\langle -\text{ICOHP} \rangle_{ref} = 1.00$  eV is somewhat arbitrary so far, and the expected inverted scenario can be attained by decreasing it. Therefore, grounded on the perspective of *flow units* [9], it is reasonable to draw a parallel between the *liquid-like* matrix and the WB atoms displayed Fig. 4, supposed to give to the NC  $\text{Zr}_{49}\text{Cu}_{49}\text{Al}_2$  a ductile character; what is also in line with the experimentally verified brittleness of the NC  $\text{Zr}_{45}\text{Cu}_{45}\text{Al}_{10}$  [23] if one look at the increased amount of SB atoms in Fig. 4(f) when compared to Fig. 4(c).

The final issue to be addressed is atomic mobility and its connection to the structural/chemical heterogeneity revealed by the ML-predicted  $\langle -\text{ICOHP} \rangle$  values. For this, it was planned a set of additional straightforward CMD simulations under the scope of mechanical loading; a basic assessment to look at the ability of the predicted bond

strengths to provide effective insights into flow mechanisms of MGs, since it is expected that WB atoms are more susceptible to atomic rearrangements. As introduced, the four MGs listed in Table II were chosen motivated by two key aspects of the experimental study reported in Ref. 23. Firstly, the authors demonstrated that the samples are homogeneous amorphous alloys before mechanical loading – i.e., they are free of nanocrystals in their microstructure. Secondly, the samples were subjected to uniaxial compression, a mechanical load test with a constrained geometry that simplifies its computational modeling. Hence, the corresponding CMD simulations were carried out for all NCs and they are quite consistent – all details are explained in the Supporting Information; including a valid justification for the restricted analyses of the resulting stress-strain curves to the onset of plastic deformation (to up to 5% strain).

Without claiming to make quantitative predictions on the rheology of these MGs, the mean-squared displacements perpendicular to the loading direction ( $\text{MSD}_{YZ}$ ) – averaged over atoms in each group – were used to gain a qualitative view of atomic mobility upon uniaxial compression up to 5% strain, as shown in Fig. 5. Remarking that in the corresponding CMD simulations, the material is increasingly compressed at a rate of  $1 \times 10^7$  s $^{-1}$ , hence

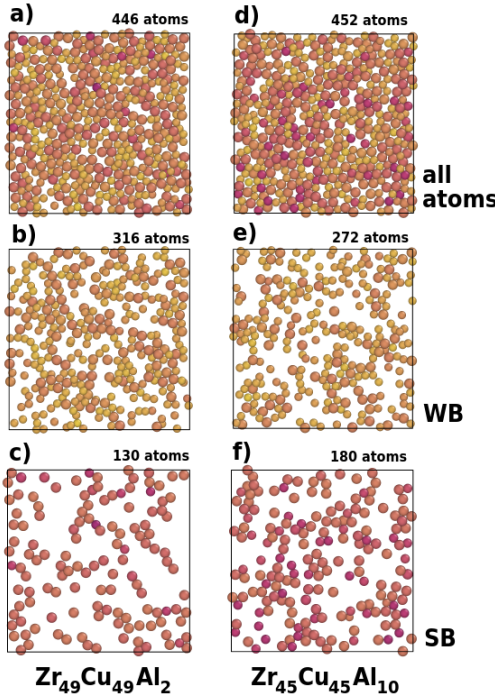


FIG. 4. Top view ( $xy$  plane) of spatial distributions of weakly bonded (WB) and strongly bonded (SB) atoms within representative  $2.5 \text{ \AA}$  slabs taken from two NCs of the ZCA alloy. Each sphere stands for an atom colored according to its  $\langle -\text{ICOHP} \rangle$  value following the same scale in Fig. 3. Groupings of atoms are based on  $\langle -\text{ICOHP} \rangle_{ref} = 1.00 \text{ eV}$  (see text).

each nanosecond in that figure corresponds to 1% strain in the corresponding stress-strain curves plotted in Fig. S32. With respect to the MSDs plots in Fig. 5, it is clear that Cu atoms (almost all the WB) present differentiated mobility upon compression in all NCs (see also Fig. S38), whereas – contrary to expectations – the smaller fraction of WB Zr atoms presented lower mobility together with the remaining SB atoms (see Table II). So, from the distributions for the Zr–Cu interactions shown in Fig. 3, it can be suggested that these WB Zr atoms have intermediate propensity to *bond exchange*, playing a key role in the interface between the *liquid-like* matrix and the *solid-like* portion of the solid; contributing the viscoelastic behavior and internal friction during the flowing process in the real material. Of course, it must be scrutinized in future studies with long time scale CMD simulations, but is out of the scope of this work. Regarding the effect of microalloying of Al, another distinct feature evidenced in Fig. 5 (and in Fig. S38) is that all the computed  $\text{MSD}_{YZ}$  values gradually decrease as Al content increases. This is consonant with the marked decrease of Zr–Cu and increase of Zr–Al interactions pointed in Fig. 3 and, in turn, is also consistent with the increase of brittleness verified experimentally in the same series of NCs, as reported in Ref. 23; supporting the common idea that the formation of stronger metal–metalloid bonds in these MGs tend to resist shear. A final remark regards

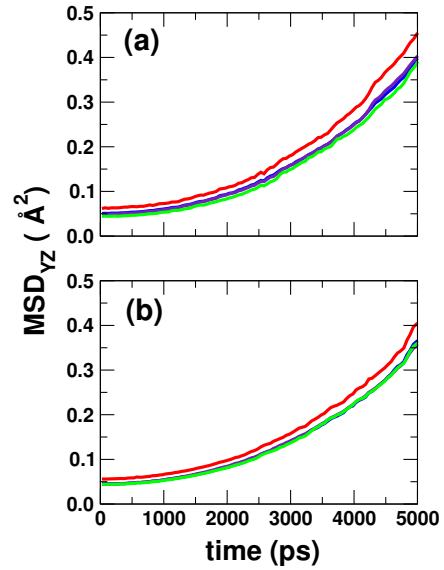


FIG. 5. Averaged mean-squared displacement components perpendicular to the loading direction ( $\text{MSD}_{YZ}$ ) computed along the uniaxial compression CMD simulations up to 5% strain for the 10000-atoms cells of the NCs (a)  $\text{Zr}_{49}\text{Cu}_{49}\text{Al}_2$ , and (b)  $\text{Zr}_{45}\text{Cu}_{45}\text{Al}_{10}$ . Groups are the same listed in Table II ( $\langle -\text{ICOHP} \rangle_{ref} = 1.00 \text{ eV}$  (see text)); red, blue, purple, and green lines stand for groups  $\text{Cu}_{WB}$ ,  $\text{Zr}_{WB}$ ,  $\text{Zr}_{SB}$ , and  $\text{Al}_{SB}$ , respectively. Groups with less than 15 atoms are ignored (see Supporting Information).

the partition criterion  $\langle -\text{ICOHP} \rangle_{ref} = 1.0 \text{ eV}$  used in Figs. 4 and 5. As shown in Figs. S39 to S42, it has yielded more reasonable connection between atomic mobility and the structural/chemical heterogeneity revealed by the ML-predicted  $\langle -\text{ICOHP} \rangle$  values.

#### IV. SUMMARY AND CONCLUSIONS

In conclusion, a ML-based approach has been used to predict -ICOHP values for chemical interactions in realistic structural models of MGs containing thousands of atoms with the accuracy of first-principles DFT calculations. Primarily, it brought an unprecedented “big picture” view of bond strengths between atoms in MGs of a prototypical alloy system and, furtherly, it provided essential differentiating criteria for the identification of bonding situations in these systems. Atom categorization is a key component in atomistic studies of properties of MGs and here, a simple per-atom index derived from the computed -ICOHP values was used. It is important to note that it holds a superior chemical sense if compared to commonly used estimators of local structure – like Voronoi polyhedrons and common neighbor analysis (CNA) – it enabled consistent separation between weakly and strongly bonded atoms as well as the detection of distinguished atomic flow response to uniaxial mechanical loading (compression) in the CMD simulations. Since

-ICOHP values are not the only quantum-mechanical indicators of bonding in materials that can be learned [43], future research focused on relaxation dynamics in MGs will certainly benefit from the findings reported in the present work.

## ACKNOWLEDGMENTS

The author is especially thankful to Prof. Gábor Csányi from University of Cambridge, UK for providing valuable guidelines and suggestions on the implementation of the ML model. Many thanks for fruitful discussions to Prof. Jichao Qiao from Northwestern Polytechni-

cal University, China. The author also acknowledges a fellowship from the São Paulo State Research Foundation (FAPESP; grant 2016/12319-0) and thanks UFSCar and Prof. José P. Rino for support. This work used the Petaflop computing facilities and associated support services of SDumont, provided by the Brazilian National Laboratory for Scientific Computing (LNCC) in Petrópolis, RJ. It also has to be pointed that a fraction of the CMD simulations (about 20%) were carried out using the high-performance computing facilities and associated support services of the National Center for High Performance Computing in São Paulo (CENAPAD-SP), which is also acknowledged.

---

[1] W. Klement, R. H. Willens, and P. Duwez, *Nature* **187**, 869 (1960).

[2] D. H. Milanez, L. I. L. Faria, D. R. Leiva, C. S. Kiminami, and W. J. Botta, *J. Alloys Compd.* **716**, 330 (2017).

[3] M. Chen, *NPG Asia Mater.* **3**, 82 (2011).

[4] W. Jiao, P. Liu, H. Lin, W. Zhou, Z. Wang, T. Fujita, A. Hirata, H.-W. Li, and M. Chen, *Chem. Mat.* **29**, 4478 (2017).

[5] Z. Mahbooba, L. Thorsson, M. Unosson, P. Skoglund, H. West, T. Horn, C. Rock, E. Vogli, and O. Harrysson, *Appl. Mater. Today* **11**, 264 (2018).

[6] N. Li, J. Zhang, W. Xing, D. Ouyang, and L. Liu, *Mater. & Design* **143**, 285 (2018).

[7] J. J. Krizic, *Adv. Eng. Mater.* **18**, 1308 (2016).

[8] J. C. Qiao, Q. Wang, J. M. Pelletier, H. Kato, R. Casalini, D. Crespo, E. Pineda, Y. Yao, and Y. Yang, *Prog. Mater. Sci.* **104**, 250 (2019).

[9] Z. Wang and W.-H. Wang, *National Science Review* **6**, 304 (2018).

[10] H. B. Yu, K. Samwer, W. H. Wang, and H. Y. Bai, *Nature Comm.* **4**, 2204 (2013).

[11] H. B. Yu, W.-H. Wang, H. Y. Bai, and K. Samwer, *National Science Review* **1**, 429 (2014).

[12] J. C. Qiao and J. M. Pelletier, *J. Mater. Sci. Technol.* **30**, 523 (2014).

[13] J. C. Qiao, Q. Wang, D. Crespo, Y. Yang, and J. M. Pelletier, *Chin. Phys. B* **26**, 016402 (2017).

[14] H. B. Yu, R. Richert, and K. Samwer, *Sci. Adv.* **3**, e1701577 (2017).

[15] Y. Q. Cheng, E. Ma, and H. W. Sheng, *Phys. Rev. Lett.* **102**, 245501 (2009).

[16] P. Hohenberg and W. Kohn, *Phys. Rev.* **136**, B864 (1964).

[17] W. Kohn and L. J. Sham, *Phys. Rev.* **140**, A1133 (1965).

[18] R. Dronskowski and P. E. Blöchl, *J. Phys. Chem.* **97**, 8617 (1993).

[19] M. C. Li, M. Q. Jiang, G. Ding, Z. H. Peng, F. Jiang, L. He, and J. Sun, *J. Non-Cryst. Solids* **468**, 52 (2017).

[20] W. Jiao, X. L. Wang, S. Lan, S. P. Pan, and Z. P. Lu, *Appl. Phys. Lett.* **106** (2015), 10.1063/1.4908122.

[21] S. Pauly, G. Liu, S. Gorantla, G. Wang, U. Kühn, D. H. Kim, and J. Eckert, *Acta Mater.* **58**, 4883 (2010).

[22] T. C. Pekin, J. Ding, C. Gammer, B. Ozdol, C. Ophus, M. Asta, R. O. Ritchie, and A. M. Minor, *Nature Mater.* **10**, 2445 (2019).

[23] G. Kumar, T. Ohkubo, T. Mukai, and K. Hono, *Scripta Mater.* **57**, 173 (2007).

[24] H. W. Sheng, W. K. Luo, F. M. Alamgir, J. M. Bai, and E. Ma, *Nature* **439**, 419 (2006).

[25] C. C. Yuan, F. Yang, X. K. Xi, C. L. Shi, D. Holland-Moritz, M. Z. Li, F. Hu, B. L. Shen, X. L. Wang, A. Meyer, and W. H. Wang, *Mater. Today* (2019), 10.1016/j.mattod.2019.06.001.

[26] V. L. Deringer, A. L. Tchougréeff, and R. Dronskowski, *J. Phys. Chem. A* **115**, 5461 (2011).

[27] S. Maintz, V. L. Deringer, A. L. Tchougréeff, and R. Dronskowski, *J. Comp. Chem.* **34**, 2557 (2013).

[28] S. Maintz, V. L. Deringer, A. L. Tchougréeff, and R. Dronskowski, *J. Comp. Chem.* **37**, 1030 (2016).

[29] S. Maintz, M. Esser, and R. Dronskowski, *Acta Phys. Pol. B* **47**, 1165 (2016).

[30] A. P. Bartók, R. Kondor, and G. Csányi, *Phys. Rev. B* **87**, 184115 (2013).

[31] G. Csányi, “libatoms.org,” (2019).

[32] S. Plimpton, *J. Comp. Phys.* **117**, 1 (1995).

[33] H. W. Sheng, “Eam potentials,” (2011).

[34] P. Giannozzi *et al.*, *J. Phys.: Cond. Matter* **21**, 395502 (2009).

[35] P. Giannozzi *et al.*, *J. Phys.: Cond. Matter* **29**, 465901 (2017).

[36] P. E. Blöchl, *Phys. Rev. B* **50**, 17953 (1994).

[37] A. D. Corso, *Comp. Material Science* **95**, 337 (2014).

[38] J. P. Perdew, K. Burke, and M. Ernzerhof, *Phys. Rev. Lett.* **77**, 3865 (1996).

[39] H. J. Monkhorst and J. D. Pack, *Phys. Rev. B* **13**, 5188 (1976).

[40] C. F. Bunge, J. A. Barrientos, and A. Bunge, *Data Nucl. Data Tables* **53**, 113 (1993).

[41] C. E. Lekka and G. A. Evangelakis, *Scripta Mater.* **61**, 974 (2009).

[42] C. E. Lekka, G. Bokas, G. A. Almyras, D. G. Papageorgiou, and G. A. Evangelakis, *J. Alloys Compd.* **536**, S65 (2012).

[43] J.-Y. Raty, M. Schumacher, P. Golub, V. L. Deringer, C. Gatti, and M. Wuttig, *Adv. Mater.* **31**, 1806280 (2019).